Convergence Analysis and Tuning of a Sliding-Mode Ripple-Correlation MPPT

Alessandro Costabeber *Member, IEEE*, Matteo Carraro and Mauro Zigliotto *Member, IEEE*

***Abstract*—The development of fast Maximum Power Point Tracking (MPPT) algorithms for photovoltaic (PV) systems with high bandwidth and predictable response to irradiation transients is attractive for mobile applications and installations under fast changing weather conditions. This paper proposes the convergence analysis of a sliding-mode version of the MPPT based on ripple correlation control (RCC). The contribution of the paper is a dynamic model, useful to derive a set of design guidelines to tune the sliding-mode RCC-MPPT and achieve a desired dynamic performance under irradiation transients, without a dedicated commissioning phase. The research is based on sliding control theory and it includes both the chattering phenomena analysis and a discussion on the effects of reactive parasitic elements in the PV module. The proposed analysis and design have been validated by Matlab simulations first and then with experimental tests on a $35\,\mathrm{W}$ panel with a boost converter charging a $24\,\mathrm{V}$ battery. The results support the effectiveness of the proposed modelling procedure and design guidelines, showing good agreement between the model prediction and the experimental transient response.**

***Index Terms*—Photovoltaic, Efficiency, Sliding mode control, Modelling, MPPT**

I. Introduction

A MAXIMUM Power Point Tracking algorithm should track any variation in solar irradiation, temperature or system parameters with minimum delay, maximising the total energy harvested from the PV system. The tracking becomes critical for PV plants installed in locations with fast changing weather conditions [1], applications like electric solar vehicles [2] or PV generation for auxiliary services or range extension in commercial cars, boats or airplanes. In these cases, the PV system undergoes frequent transients, due to turn in the weather or shading objects (buildings, trees, poles etc.).

The most common MPPT methods in literature are P&O (perturb and observe) [3], [4], hill climbing [5], incremental conductance [6], fractional voltage [7] and ripple correlation control [8]. A comprehensive review and comparison of the most popular MPPT methods can be found in [9]–[11], where the different control solutions are classified in terms of complexity, true MPPT capability, number of sensors and effect of parametric variations. The cited papers include some comparisons in terms of convergence speed, but the inherent non-linearity of MPPT controllers often pushes towards a heuristic approach. Therefore, it is not always evident whether the dynamic performance of each controller is optimised or not. In practical implementations, the maximisation of the convergence speed usually requires a commissioning phase to adapt the controller to the specific application. This paper is an attempt to provide a more rigorous approach to MPPT dynamic response design, and applies to systems where a fast and predictable response is desirable. The sliding-mode RCC-MPPT has been selected for its inherent fast response, ease of implementation even with analogue circuits and absence of external disturbances to the operating point of the PV system. The technique was first proposed in [12], where RCC was applied to detect the maximum power operating point on the power-voltage curve of a photovoltaic panel. Several relevant features have been addressed in this first paper, such as stability and limitations introduced by the parasitic capacitance. An insight on RCC-MPPT is found in [13], where the authors review several possible implementations, while a detailed digital RCC-MPPT implementation can be found in [14]. From the theoretical point of view, techniques in [12], [13], [14] belong to Extremum-Seeking controls (ESC), as demonstrated in [15]. The relevance of RCC is also confirmed by its multidisciplinary nature [8], [16]. Since the original version of [12], several variations have been proposed. Among them, [17] uses the voltage ripple at twice the line frequency in single phase inverters to drive the ripple correlation control and an alternative is proposed in [18], where the correlation is a XOR port, receiving in input the squared voltage and power ripples, simplifying the hardware. The solution proposed in this paper modifies the original scheme in [12] to turn it into a sliding-mode controller whose dynamics can be modelled under appropriate hypotheses. Particular emphasis is placed in the properties of stability and convergence of the proposed sliding-mode RCC-MPPT, with the aim of providing a set of guidelines to predict the dynamic response to solar transients, without post-characterization or manual tuning.

The paper is organised as follows: Sect.II recalls the basics of RCC-MPPT, and presents the proposed sliding mode scheme. Sect.III analyses the model of the PV panel used throughout the paper and the influence of reactive parasitics. The theoretical formalization of the control is in Sect.IV, with particular emphasis on convergence and stability. Sect.V derives a simplified analysis of the chattering phenomena, based on the describing function method. The simulation and experimental results that validate the outcomes of Sect.IV and Sect.V are presented in Sect.VI. Finally, Sect.VII summarises the procedure required for the practical implementation of the sliding-mode RCC-MPPT.

Alessandro Costabeber is with the Department of Electrical and Electronic Engineering, University of Nottingham, Nottingham NG7 2RD, UK Email: alessandro.costabeber@nottingham.ac.uk.

Matteo Carraro and Mauro Zigliotto are with the Department of Technique and Management of Industrial Systems (DTG), University of Padova, Italy. Phone +39 (0444) 998818 Email: mauro.zigliotto@unipd.it.

II. Review of RCC-MPPT basics and Sliding-Mode RCC-MPPT

The MPPT scheme is applied to a battery charger from single PV module. The converter is a boost with direct duty cycle control, operating in CCM (Continuous Conduction Mode). The proposed analysis can be extended to any other control configuration, i. e. with current loop and/or voltage loop.

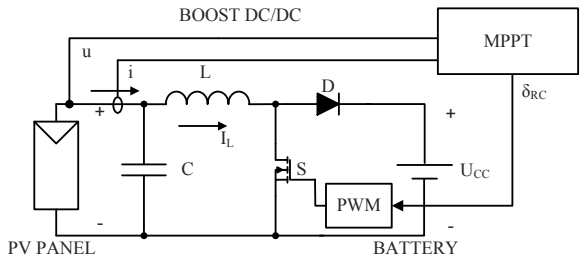

Fig. 1. Photovoltaic battery charger setup.

According to [13], the RCC-MPPT drives the boost input voltage toward the MPP by zeroing the power gradient with respect to the voltage. The generic $(p-u)$ curve of a PV module reported in Fig.2 indicates that the derivative of the power with respect to the voltage is positive before the MPP, negative after it and of course zero at the MPP itself. If δ_{RC} is the duty cycle of the boost converter imposed by the RCC-MPPT, then a straightforward control law for MPP tracking is:

$$\delta_{RC} = \gamma \int_0^t \frac{\partial p}{\partial u} dt \tag{1}$$

where γ is a real gain. For a boost converter operating in CCM, the reciprocal of the conversion ratio is $N = u/U_{CC} = 1 - \delta_{RC}$. According to (1), the system converges to the MPP when $\gamma < 0$. In fact, when the derivative is positive, δ_{RC} decreases and the input voltage u increases, moving the operating point toward the MPP. The opposite happens if the derivative is negative.

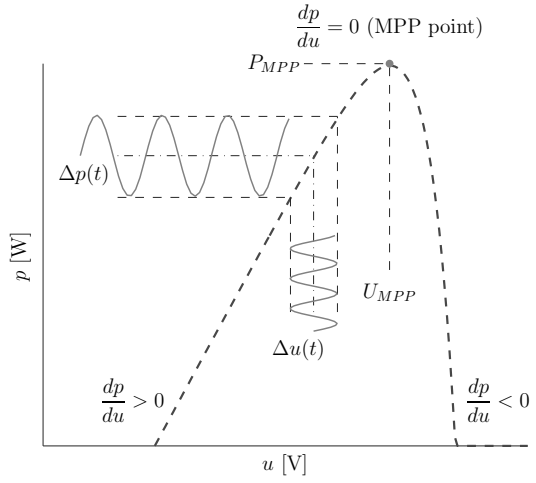

Fig. 2. General representation of the steady state $p-u$ curve $p(t) = f(u(t), I_{SH})$ of a PV panel under constant irradiation.

The same information contained in the derivative in (1) can be found in the correlation function $\varepsilon(t)$ [18], reported in (2). The original solution proposed in [13] is similar, except for the absence of the two sign functions before the product.

$$\varepsilon(t) = \text{sign}\Big(\frac{\partial p}{\partial t}\Big)\text{sign}\Big(\frac{\partial u}{\partial t}\Big) \Rightarrow \delta_{RC} = \gamma \int_0^t \varepsilon(t) dt \tag{2}$$

Adopting the small signal approximation, the AC power and voltage disturbances Δp and Δu in Fig.2 can be used to replace the power and voltage time derivatives, and they are extracted by high-pass filters (HPFs), as in Fig.3. In the following analysis, the AC disturbances are considered as sinusoidal, for the sake of simplicity. Starting from the correlation (2), the RCC-MPPT scheme can be turned into the sliding-mode controller proposed in this paper by interposing a low-pass filter (LPF) and a sign function before the integral action:

$$\delta_{RC} = \gamma \int_0^t \text{sign}(\varepsilon_F(t)) dt \tag{3}$$

where $\varepsilon_F(t)$ is the low-pass filtered correlation. Two possible implementation schemes are reported in Fig.3. Stability and convergence analysis will be provided for the upper side scheme of Fig.3. The second scheme has a simpler implementation while maintaining the same dynamic response, is used in the experimental setup.

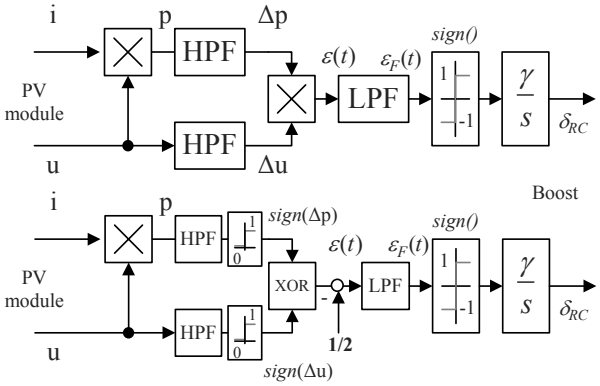

Fig. 3. Sliding-mode RCC-MPPT schemes (Top: based on [13] Bottom: based on [18]).

III. PV panel modelling

The PV module has been modelled in steady state adopting the lumped parameters scheme in Fig.4a, including parasitic series and shunt resistances.

$$i = I_{SH} - I_s \left(\mathrm{e}^{\dfrac{u + R_S i}{\eta V_T N_c}} - 1 \right) - \frac{u + R_S i}{R_P} \tag{4}$$

where I_{SH} is the photo-generated current, or short circuit current, which depends on solar irradiation, I_s is the inverse saturation current, u and i are voltage and current of the module, N_C the number of cells, R_S and R_P the total series and shunt resistances, η is the ideality factor of the junction

and V_T the temperature equivalent voltage $V_T = KT/q$ where $K = 1.38 \times 10^{-23}\,\mathrm{J/^\circ K}$ is the Boltzmann's constant, T is the temperature in K and q the charge of the electron. A more detailed model includes a series inductor L_P, accounting for cells bonding and cables, and a shunt capacitor C_P, accounting for the non-linear cells junction capacitance and the bypass diode capacitance, if present. The inductance L_P can be considered constant, the capacitor depends irradiation and operating voltage. The model is always intended as a small signal model, valid in a specific operating point and is reported in Fig.4b, where R_P and R_S are neglected.

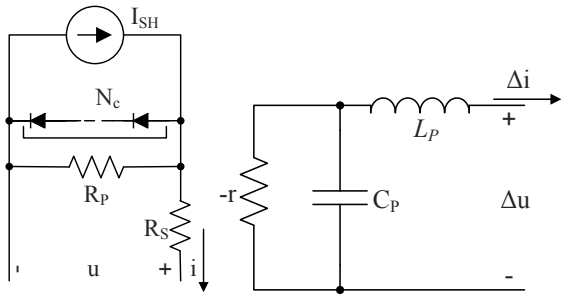

Fig. 4. Fig.4a: Steady-state PV model and Fig.4b: PV small-signal linearised dynamic model including reactive parasitics.

The differential resistance r can be obtained by linearising (4) around a generic operating point (U_0, I_{SH}):

$$r = \left(\frac{\partial u}{\partial i}\right)\Big|_{U_0,I_{SH}} = -\frac{\eta V_T N_c}{I_s}\mathrm{e}^{-\dfrac{U_0}{\eta V_T N_c}} \tag{5}$$

The dynamic behaviour is described by the transfer function between Δu and Δi, bearing in mind the dependence of the capacitance on both the operating voltage and the irradiation condition $C_P(U_0, I_{SH})$ [19]:

$$-Y(s) = \frac{I(s)}{U(s)}\Big|_{U_0,I_{SH}} = \frac{1}{r}\frac{1 - srC_P}{1 - s\dfrac{L_P}{r} + s^2 L_P C_P} \tag{6}$$

$Y(s)$ represents the input admittance and in absence of parasitics it is the reciprocal of the differential resistance r.

The small-signal transfer function $H(s) = \mathcal{L}(\Delta p)/\mathcal{L}(\Delta u) \triangleq P(s)/U(s)$, around a specific operating point (U_0, I_0, I_{SH}), can be obtained as follows:

$$\begin{aligned} &p = ui = (U_0 + \Delta u)(I_0 + \Delta i) \rightarrow \Delta p = I_0 \Delta u + U_0 \Delta i \\ &H(s) = \frac{P(s)}{U(s)}\Big|_{U_0,I_{SH}} = I_0(1 + Y(s)R_0), \quad R_0 = -\frac{U_0}{I_0} \end{aligned} \tag{7}$$

And by defining:

$$M = \frac{R_0}{r}, \omega_0 = \frac{1}{\sqrt{L_P C_P}}, \xi = -\frac{1}{2r}\sqrt{\frac{L_P}{C_P}} \tag{8}$$

The dynamic relation between the PV power and voltage ripples becomes:

$$\begin{aligned} H(s) &= \frac{I_0\left((1-M) + \dfrac{s}{\omega_0}\left(2\xi - \dfrac{1}{2\xi}M\right) + \dfrac{s^2}{\omega_0^2}\right)}{1 + 2s\dfrac{\xi}{\omega_0} + \dfrac{s^2}{\omega_0^2}} \\ H(s) &= H_P(s) + H_{LC}(s), \quad H_P(s) = I_0(1-M) \end{aligned} \tag{9}$$

where all the terms are functions of the operating point (U_0, I_{SH}). $H(s)$ is expressed as the sum of the ideal H_P and a function H_{LC} that accounts for the parasitics. With reference to Fig.3, the equilibrium is reached when the mean value of the correlation $\varepsilon(t)$ equals zero. That is, either the high pass filtered AC disturbances are phase-shifted by $\pm\pi/2\,\mathrm{rad}$ or the power disturbance is zero. In absence of parasitics, $H_P(s) \equiv H(s)$, and the only possible equilibrium is when the power disturbance goes to zero, that is:

$$H(s) = I_0(1-M) = 0 \rightarrow M = 1 \rightarrow r = R_0 \tag{10}$$

Equation (10) shows that, in absence of parasitics, the transfer function is a pure gain depending on the operating point, and the only possible equilibrium for the RCC-MPPT is when the gain equals zero. As a step further, it is possible to add the effect of $C_P(U_0, I_{SH})$. Rearranging (9), $H(s)$ becomes:

$$H_{LC}(s) = -\frac{I_0 M}{2\omega_0 \xi}s \rightarrow H(s) = I_0\left(1 - M + sMrC_P\right) \tag{11}$$

The linearised transfer function has a single zero whose time constant depends on the operating point. The magnitude of Δp cannot be zero, regardless of the ripple frequency. Therefore, the RCC-MPPT equilibrium, corresponding to the operating point where the mean value of $\varepsilon(t)$ is equal to zero (i.e. the integrator in (2) is in steady state), is possible only when the phase shift between Δp and Δu is $\pi/2\,\mathrm{rad}$. This is equivalent to the condition $M = 1$, as in the ideal case. This confirms that C_P does not affect the convergence of the RCC-MPPT to the ideal point. From a different perspective, the same result was obtained in [12], where $p - u$ RCC was proposed as an alternative to $p - i$ RCC for its insensitivity to the capacitance C_P. The research in [12] also highlighted the implicit effect of the ripple frequency in (11), that is that all the transfer functions calculated for a varying operating point have a phase diagram converging to $-\pi/2\,\mathrm{rad}$. Therefore, the greater the ripple frequency, the lower the sensitivity of the MPPT and it is difficult to distinguish the MPP. Conversely, the inclusion of the inductor L_P leads to a different MPP. The equilibrium point is still where the phase of $H(s)$ is $\pm\pi/2\,\mathrm{rad}$, but that point is in general different from the MPP point computed in absence of parasitics. The new equilibrium point is obtained by finding the value of M that makes $\Re(H(j\omega_{AC})) = 0$, i.e. Δp and Δu are in quadrature:

$$M = \left(1 - \frac{\omega_{AC}^2}{\omega_0^2}\right)^2 + \left(2\xi\frac{\omega_{AC}}{\omega_0}\right)^2 \tag{12}$$

where M, ω_0 and ξ depend on the operating point (U_0, I_{SH}). The implicit form of (12) calls for a numerical

solution to find the equilibrium point, as a function of the AC disturbance frequency ω_{AC} [19]. The relevant information contained in (12) is that an equilibrium error is unavoidable in presence of both C_P and L_P, and the only possible action is to reduce the ripple frequency to values where the impact of L_P can be neglected. If C_P was independent from the operating point, a compensation of the phase shift would be possible, but its non-linear nature prevents this opportunity. A further theoretical extension of these concepts can be found in Sect.IV and in the experimental evidences reported in Sect.VI.

IV. MPPT CONVERGENCE AND STABILITY ANALYSIS

This section presents stability and convergence analysis of the first Sliding-Mode RCC-MPPT scheme in Fig.3. The first subsection describes voltage and power ripples, including the effect of reactive parasitics described in the previous section. The remaining subsections focus on the trajectory of the operating point during transients, proving the stability of the control system and estimating the convergence time for dynamic design purposes.

A. Control properties

The overall analysis is based on the following assumptions:

- The boost converter operates in CCM, connected to the battery U_{CC}. Naming $G(s)$ the transfer function between the duty cycle δ_{RC} and the PV voltage u, we assume $G(s) \approx -U_{CC}$, i.e. the DC gain replaces the input filter dynamic. This is acceptable when the dynamic of the input filter is faster than the desired MPPT response. The full $G(s)$ will be used in the chattering analysis.
- The disturbance used to extract the information on the $p-u$ curve is the input voltage ripple, modelled as an additive sinusoidal disturbance Δu.
- The extraction of power ripple Δp and voltage ripple Δu is based on two high pass filters (HPF), HPF_1 and HPF_2. Their cut-off frequencies are ω_{HPF1} and ω_{HPF2}.
- The filtered power Δp and voltage Δu are named O_1 and O_2. ε is the correlation, then filtered by a low pass filter (LPF) with cut-off frequency ω_{LPF}. The residual AC ripple after filtering is assumed negligible. The $sign()$ block output is integrated by the RCC-MPPT integrator with gain γ.

Overall, the previous assumptions allow to consider the simplified scheme in Fig.5, where:

$$\begin{cases} \Delta u = u - U_0 = A\,\sin(\omega_{AC} t) \\ \Delta p_{LC} = A k_P k_{LC} \sin(\omega_{AC} t + \varphi_{LC}) \\ \Delta p_P = A k_P \sin(\omega_{AC} t + \varphi_P) = \Delta u \dfrac{\partial f(u(t))}{\partial u}\Big|_{U_0, I_{SH}} \\ U_0 = (1-\delta_{RC}) U_{CC} \\ P_0 = f(U_0, I_{SH}) \end{cases} \tag{13}$$

Where ω_{AC} is the voltage perturbation frequency, A its amplitude, $k_{LC} = |H_{LC}(j\omega_{AC})|$, $\varphi_{LC} = \angle H_{LC}(j\omega_{AC})$, $k_P = |H_P(j\omega_{AC})|$ and $\varphi_P = \angle H_P(j\omega_{AC})$. Defining the attenuations $k_{HFi} = |H_{HFi}(j\omega_{AC})|, i = 1,2$ and the phases

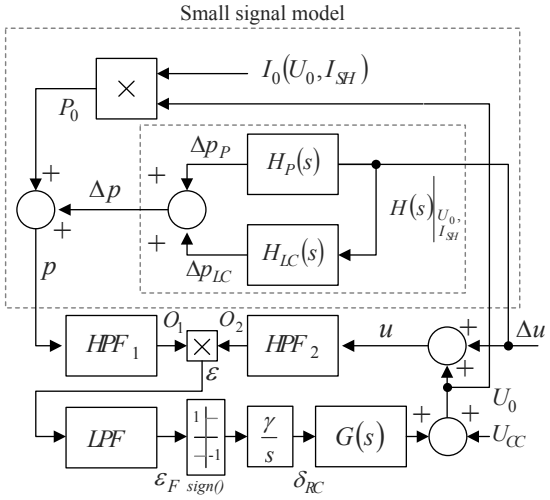

Fig. 5. MPPT detector linearised around a generic operating point, including reactive parasitics effect.

$\varphi_{HFi} = \angle H_{HFi}(j\omega_{AC}), i = 1,2$ introduced by HPFs, the mean value of the correlation $\varepsilon(t)$ is computed as:

$$\begin{aligned} \varepsilon_F(t) = &\frac{A^2}{2} k_{HF1} k_{HF2} k_P \cos(\varphi_{HF1} - \varphi_{HF2} + \varphi_P) \\ &+ \frac{A^2}{2} k_{HF1} k_{HF2} k_{LC} \cos(\varphi_{HF1} - \varphi_{HF2} + \varphi_{LC}) \end{aligned} \tag{14}$$

In absence of parasitics, i.e. $k_{LC} = 0$, the natural filters tuning is $\mathrm{HPF}_1 = \mathrm{HPF}_2 = \mathrm{HPF}$, which leads to $\varepsilon_F(t) = 0$ in the MPP operating point ($k_P = 0$). Including the parasitic components, the filtered output error $\varepsilon_F(t)$ can be written as

$$\varepsilon_F(t) = \frac{A^2 k_{HF}^2 k_P}{2} \cos(\varphi_P) + \frac{A^2 k_{HF}^2 k_{\mathrm{LC}}}{2} \cos(\varphi_{LC}) \tag{15}$$

and the equilibrium condition becomes:

$$k_P \cos(\varphi_P) + k_{LC} \cos(\varphi_{LC}) = 0 \tag{16}$$

Equation (16) derives from (12) by placing $\Re[H(s)] = 0$, $s = j\omega_{AC}$, i.e. by imposing, at the equilibrium point, the condition of quadrature between power and voltage ripples. Compared to (12), (16) clearly highlights the wrong convergence occurring when the parasitic reactance at frequency ω_{AC} cannot be neglected. In this case, the system might converge to the correct ideal point (M=1), or either to a point below (M<1) or above (M>1) the ideal point, depending on which of the following conditions is verified at ω_{AC}:

$$\begin{aligned} &M = 1 \text{ if } k_{LC} \cos(\varphi_{LC}) = 0 \rightarrow \varphi_{LC} = \frac{\pi}{2} + k\pi \\ &M > 1 \text{ if } k_P = k_{LC} \cos(\varphi_{LC}) \\ &M < 1 \text{ if } k_P = -k_{LC} \cos(\varphi_{LC}) \end{aligned} \tag{17}$$

with $k \in \mathbb{Z}$ and all the parameters dependent on the operating point. Equation (16) can be rewritten assuming the additional degree of freedom of different high pass filters for power and voltage ripples measurements. Let $\Delta\varphi = \varphi_{HF1} - \varphi_{HF2}$, the equilibrium condition becomes:

$$k_P \cos(\Delta\varphi + \varphi_P) + k_{LC} \cos(\Delta\varphi + \varphi_{LC}) = 0 \tag{18}$$

The ideal MPP (i. e. $M = 1$) is reached by forcing $\cos(\Delta\varphi + \varphi_{LC}) = 0$, that is:

$$\Delta\varphi = \frac{\pi}{2} + k\pi - \varphi_{LC} \tag{19}$$

where φ_{LC} is the phase shift due to the parasitics under the ideal MPP condition with $M = 1$. Equation (19) shows that a phase shift introduced in the measurement filters can be used to compensate the effect of the parasitic components. As anticipated in Sect.III, the compensation would be possible only if C_P was constant, while in practice it varies with operating voltage and irradiation. Consequently, the only countermeasure to attenuate the effect of parasitics is to reduce the switching frequency to values where L_P is negligible.

B. Convergence and stability proof

To prove the stability and convergence properties of the system, the scheme in Fig.5 has been simplified as in Fig.6, which is based on the assumptions that the operating frequency allows to neglect reactive parasitics and that all the measurement filters, including the boost converter input filter, do not affect the dynamic of the operating point during irradiation transients. Once the RCC-MPPT is designed for

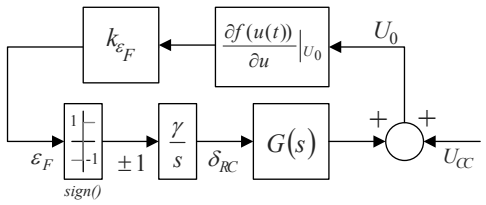

Fig. 6. Simplified scheme for stability and convergence analysis.

a specific response, the choice of the filters must respect these hypotheses. The idea behind these assumptions is to decouple the fast AC sensing dynamics from the slow dynamics of the operating point. The result is a single-state non-linear system, with two non-linearities, i. e. the sign function and the voltage derivative $\left.\frac{\partial f(u(t))}{\partial u}\right|_{U_0}$. Equation (14) can be rewritten as:

$$\varepsilon_F(t) = \frac{A^2}{2} k_{HF}^2 \left.\frac{\partial f(u(t))}{\partial u}\right|_{I_{SH},U_0} = K_{\varepsilon_F} \left.\frac{\partial f(U_0)}{\partial U_0}\right|_{I_{SH}} \tag{20}$$

Under these hypotheses, the system can be modelled as an elementary sliding-mode controller [20], where the state x is the duty cycle δ_{RC}, the sliding surface $\sigma(x,t)$ is the filtered correlation $\varepsilon_F(t)$ and the state derivative changes depending on sign of the sliding surface:

$$\begin{cases} \dot{x} = g(x,t) = \dot{\delta}_{RC} = \gamma \mathrm{sgn}(\varepsilon_F) \\ g(x,t) = \begin{cases} g^+(x,t) & if \quad \sigma(x,t) > 0 \\ g^-(x,t) & if \quad \sigma(x,t) < 0 \end{cases} \\ \sigma(x,t) = \varepsilon_F(t) \quad \text{sliding surface} \end{cases} \tag{21}$$

In the model, the concept of sliding surface collapses to a sliding line and the dynamics in sliding regime collapses to a motion around a single point, the state corresponding to $\sigma = 0$. This state automatically becomes also the equilibrium point, and corresponds to the maximum power point. The existence of the sliding mode, the reachability of the sliding point and the stability of the motion around the point are all verified if:

$$\sigma\dot{\sigma} = \varepsilon_F(t)\frac{d\varepsilon_F(t)}{dt} < 0 \qquad \forall\delta_{RC} \tag{22}$$

meaning that for any state x, the state velocity is directed toward the sliding line. The inequality (22) can be verified by substituting the definition of σ:

$$\varepsilon_F \frac{d\varepsilon_F(t)}{dt} = \varepsilon_F K_{\varepsilon_F} \left.\frac{\partial f(U_0)}{\partial U_0}\right|_{I_{SH}} \frac{dU_0}{dt} \tag{23}$$

Assuming that $dU_0/d\delta = G(j0) = -U_{CC}$ and by applying the chain differentiation rule, it follows that:

$$\frac{dU_0}{dt} = \frac{dU_0}{d\delta}\frac{d\delta}{dt} = \frac{dU_0}{d\delta}\gamma\mathrm{sgn}(\varepsilon_f) \quad \approx G(j0)\gamma\mathrm{sgn}(\varepsilon_f) \tag{24}$$

where $K_{\varepsilon_f} > 0$, $\gamma < 0$ and $G(j0) = -U_{CC} < 0$. The sign of (23) is only dependent on the sign of the second derivative of the p-u curve, and if the latter is negative for all U_0 up to the open circuit voltage, the condition (22) is verified. The sign of the second derivative can be analytically studied calculating the power p from (4), neglecting the parasitic resistances and by defining $\beta \triangleq \frac{1}{\eta V_T N_c}$. For positive operating voltages $U_0 > 0$ it follows that:

$$\frac{\partial^2 f(U_0)}{\partial U_0^2} = -\left(2\beta I_s \mathrm{e}^{\beta U_0} + \beta^2 U_0 I_s \mathrm{e}^{\beta U_0}\right) \tag{25}$$

which proves the inequality (22).

C. Convergence time estimation

The previous analysis can be further extended to derive a design criterion for the integral gain γ that guarantees an upper bound to the convergence time towards a new MPP, in response to a solar irradiation step variation. From (24) and (23), it is:

$$\sigma\dot{\sigma} = -K_{\varepsilon_F}\frac{\partial^2 f(U_0)}{\partial U_0^2} U_{CC}\gamma|\sigma| \tag{26}$$

According to (20), the second time derivative can be rewritten as:

$$\frac{\partial f^2(U_0)}{\partial U_0^2} = \frac{1}{K_{\varepsilon_F}}\frac{\partial\sigma}{\partial U_0} \tag{27}$$

By replacing (27) into (26):

$$\sigma\dot{\sigma} = -\frac{\partial\sigma}{\partial U_0} U_{CC}\gamma|\sigma| \rightarrow \frac{\sigma}{|\sigma|}\partial U_0 = -U_{CC}\gamma\partial t \tag{28}$$

When the system experiences a solar radiation step, it is now possible to calculate the convergence time from an initial MPP voltage U_i to the new MPP characterized by a voltage U_f, by integrating the right hand term of (28):

$$T = -\frac{|U_f - U_i|}{U_{CC}\gamma} \rightarrow \gamma = -\frac{|U_f - U_i|}{U_{CC}T} \tag{29}$$

The integral gain γ in (29) can be driven by the definition of a maximum convergence time. The numerator of (29) can be obtained identifying a set of relevant solar irradiation transients for the specific application. For instance, naming $U_{i,min}$ the MPP voltage at a predefined minimum solar irradiation level

$I_{SH,min}$, and $U_{f,max}$ the MPP voltage at the maximum irradiation level $I_{SH,max}$, and T_{MAX} the maximum desired convergence time, the integrator gain is:

$$\gamma = \max_{I_{SH}} \left(-\frac{|U_{f,max} - U_{i,min}|}{U_{CC} T_{MAX}} \right) \tag{30}$$

The validity of (30) will be confirmed by the experimental results of Sect.VI, despite the approximations used to derive T_{MAX}. In particular:

- The MPPT dynamic is slower than those of the measurement filters and the boost converter input filter $G(s)$.
- The reactive parasitics have been neglected, i.e. the operating frequency allows to neglect L_P.
- A range of relevant transients should be identified a priori, and the MPP locus be obtained from characterization of the PV module. The tuning of γ could also be executed online: starting from a low value, and fixing a target for T_{MAX}, a tuning algorithm could keep trace of the operating MPP voltage extremes and the correspondent powers, and periodically update the value of γ. This comes at the cost of an increased complexity of the controller.

It is worth noting that (30) is also independent from the operating temperature of the PV module. Assuming the open-circuit voltage VOC to be the only parameter varying with temperature, the MPPs locus tends to be shifted to lower voltages as the temperature increases, but the voltages difference in (30) makes the dynamic design independent from voltage shifts.

V. Simplified chattering analysis

So far, the analysis has assumed an ideal sliding motion, neglecting the chattering around the equilibrium. The chattering is now modelled as a limit cycle, adopting the *describing function* method. From the linearised scheme in Fig.5, the encircled small signal-model, the filters, the correlation and the sign can be replaced by a describing function $A(U, \omega_C)$. In Fig.7, which assumes the existence of a chattering oscillation at ω_C, the output $O_C(j\omega_C)$ is the fundamental of the square wave after the *sign* function contained in $A(U, \omega_C)$, corresponding to $4/\pi$ for any sinusoidal input. Instead, the phase of A requires a Taylor expansion of the $p - u$ curve around the MPP. Assume the voltage u to be the sum between

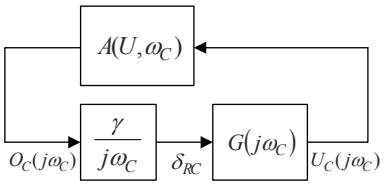

Fig. 7. Simplified scheme for chattering analysis.

U_0 (the DC equilibrium voltage) and the chattering u_C:

$$u = U_0 + U_C \sin(\omega_C t) = U_0 + u_C \tag{31}$$

By expanding the exponential (4) around U_0 and truncating the power series to the second order term, while assuming $R_S = R_P = 0$, the corresponding power results:

$$\begin{aligned} p = ui = & P_{\text{DC}} + k_1 \sin(\omega_C t) + k_2 \cos(2\omega_C t) + \cdots \\ & \cdots + k_3 \sin(3\omega_C t) \end{aligned} \tag{32}$$

P_{DC} is the average power and $k_i \, i = 1..3$ are coefficients whose explicit equations are not necessary for the analysis, that only needs to identify the component at ω_C in the correlation output. By using trigonometric identities, the only term in (32) generating ω_C after HPF and multiplication with filtered u_C is $\cos(2\omega_C t)$. The component at ω_C after correlation and LPF is:

$$\varepsilon_{f,\omega_C} = K_C \sin(\rho) \quad K_C < 0 \tag{33}$$

where $\rho = \omega_C t + \varphi_C, \varphi_C = \varphi_{HPF}(j2\omega_C) - \varphi_{HPF}(j\omega_C) + \varphi_{LPF}(j\omega_C)$. Therefore, the describing function is:

$$A(\omega_C, U) = \frac{O_C(j\omega_C)}{U_C(j\omega_C)} = -\frac{4}{\pi |U|} e^{j\varphi_C} = \frac{4}{\pi |U|} e^{j(\varphi_C + \pi)} \tag{34}$$

The oscillation condition on the module is:

$$|A(\omega_C, U)||G(j\omega_C)|\left|\frac{\gamma}{j\omega_C}\right| = 1 \rightarrow |U| = \frac{4|\gamma||G(j\omega_C)|}{\pi \omega_C} \tag{35}$$

and the corresponding phase condition becomes

$$\varphi_C + \frac{3\pi}{2} + \angle G(j\omega_C) = 2k\pi \tag{36}$$

Also the frequency of the oscillation ω_C can be directly calculated from (36), while the amplitude U_C is derived from (35).

VI. Simulation and Experimental Results

This section aims at validating the previous theoretical analysis. It begins with the experimental static and dynamic characterisation of the PV module under test. Based on the PV module data, a validation of the predicted convergence time, chattering analysis and effect of the LPF is first obtained by simulation and then confirmed by experimental results.

A. Description of the experimental setup

The experimental setup implements the scheme in Fig.1: a 35 W PV module charges a 24 V lead-acid battery with a boost converter with duty cycle driven by the sliding-mode RCC-MPPT. The implementation reflects the second scheme in Fig.3, using an XOR function as correlation block. The instantaneous power is measured with an analog multiplier IC and all the filters are op-amps based. The HPFs are first order filters, the LPF is a second order filter. Table I collects the main parameters of the system. The dynamic testing requires a controllable solar emulator, whose implementation details can be found in [21]. It is based on a matrix of 1344 LEDs, divided in 24 modules of 56 LEDs, each module driven by a dedicated buck converter with current control loop with bandwidth $B_{LED} = 2\,\text{kHz}$. The maximum power on the PV module surface has been estimated to be $P_{LED} \approx 680\,\text{W/m}^2$.

(a) (b)

Fig. 8. Fig.8a: PV module and LED solar emulator and Fig.8b: boost converter and sliding-mode RCC-MPPT analog control board.

Table I
PV MODULE AND BOOST CONVERTER PARAMETERS

BOOST Converter	
Nominal Power	$P_N = 200\,\mathrm{W}$
Output Voltage	$U_{CC} = 24\,\mathrm{V}$
Switching frequency	$f_{SW} = 220\,\mathrm{kHz}$
Boost inductor	$L = 50\,\mu\mathrm{H}$
Input capacitor	$C = 6.2\,\mu\mathrm{F}$
Input capacitor ESR	$ESR = 5\,\Omega$
PV module	
Nominal Power	$P_{PV} = 35\,\mathrm{W}$
Open circuit voltage	$V_{OC} = 19.4\,\mathrm{V}$
Short circuit current	$I_{SH} = 2.5\,\mathrm{A}$
MPP voltage	$V_{MPP} = 15.5\,\mathrm{V}$
MPP current	$I_{MPP} = 2.25\,\mathrm{A}$
Size WxLxH	$540 \times 630 \times 55\,\mathrm{mm}$

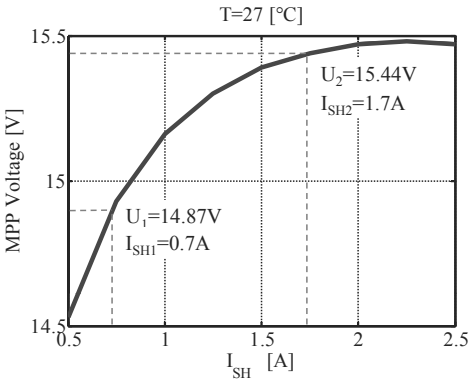

(a) MPP locus @ 27°

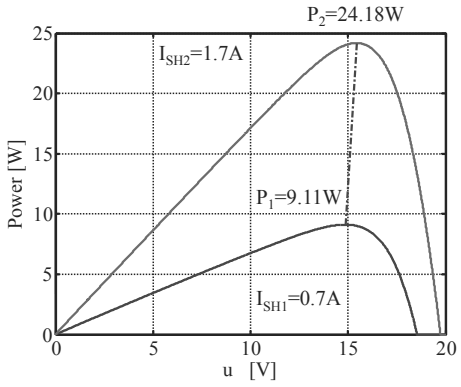

(b) Steady state $p-u$ characteristics

Fig. 9. Fig.9a: MPP locus and corresponding steady state $p-u$ characteristics in the two considered irradiation levels.

B. PV module characterization

1) Steady state model: A correct steady state experimental modelization of the PV module is necessary to obtain the MPPs locus, required to design the dynamic response of the sliding-mode RCC-MPPT with (29). The $V-I$ curve has been derived at the maximum radiated power $P_1 = 680\,\mathrm{W/m^2}$, corresponding to a short circuit current $I_{SH1} = 1.7\,\mathrm{A}$, and at the temperature $T = 40°\mathrm{C}$. The results have been fitted with a LMS (Least Mean Square) algorithm to the model in (4). The outputs of the fitting are the parasitic resistances $R_S = 0.693\,\Omega$ and $R_P = 424.3\,\Omega$ and the ideality factor $\eta = 2.04$. To experimentally validate the dynamic behaviour of the sliding-mode RCC-MPPT, a set of two transient conditions has been programmed in the solar emulator. The first is the maximum power $P_1 = 680\,\mathrm{W/m^2}$ ($I_{SH1} = 1.7\,\mathrm{A}$), the second is equal to $P_2 = 280\,\mathrm{W/m^2}$ ($I_{SH2} = 0.7\,\mathrm{A}$). According to the fitted model, the MPPT locus and the $p-u$ curves calculated at $T = 27°\mathrm{C}$ are reported in Fig.9.

2) Approximated dynamic model: An approximated dynamic identification of the PV panel can be performed to estimate the non-linear capacitor C_P. To measure C_P, the PV module has been connected to the measurement circuit proposed in [19]: a MOSFET is operated in its saturation region, driven by a gate voltage with a DC component and a small AC perturbation, with frequency $f_i = 500\,\mathrm{Hz}$. If the frequency is low enough, the inductor L_P can be neglected, and the phase shift between u and i ripple depends on the capacitor C_P. By extracting the component of the current ripple leading the voltage ripple by $\pi/2\,\mathrm{rad}$, the capacitor can be estimated for a set of operating points. An FFT has been used to filter out non-linearities caused by the PV module. Fig.10a reports the set of estimated values: As expected, the capacitor is non-linear, ranging from few hundreds of nF to few tens of μF depending on operating voltage and irradiation, for the combined effects of non-linear junction capacitance, mostly dependent on the voltage u and diffusion capacitance, mostly influenced by I_{SH}. To complete the approximated dynamic analysis, L_P has been measured connecting the PV module to the boost converter operated in open-loop. By varying the duty cycle, the $p-u$ curves at I_{SH1} and I_{SH2} have been swept, measuring for each point the voltage and power ripples Δp and Δu at the switching frequency. The phase shift between p and u has been calculated and compared with the expected value from the linearised transfer function (9), calculated at $\omega_{AC} = 2\pi f_{SW}$ for each operating point. A rough approximation of L_P has then been then found by fitting the measured phase shifts and the ones predicted with (9), resulting in $L_P = 480\,\mathrm{nH}$. The measured phase shift is reported in Fig.10b.

C. Simulations results

The first simulations validate the convergence time and chattering neglecting L_P, but including C_P. For simplicity, a constant $C_P = 0.5\,\mu\mathrm{F}$ and an average model of the boost converter are used. The ripple is emulated with an additive duty cycle disturbance set to produce the same voltage

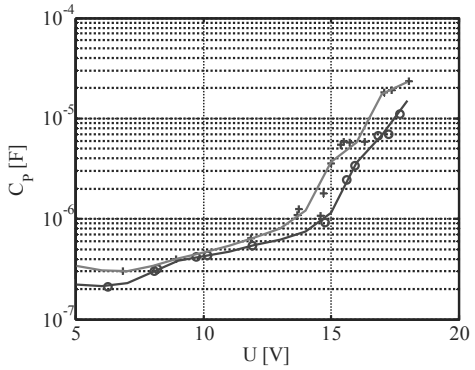

(a) Estimated non-linear capacitor

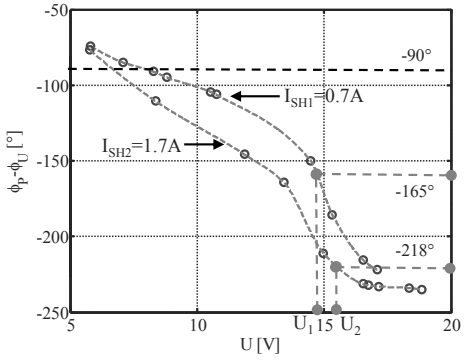

(b) Phase shift between Δp and Δu

Fig. 10. (a) Estimated non-linear capacitor C_P ($I_{SH1} = 0.7A$ indicated with circles, $I_{SH2} = 1.7A$ indicated with crosses) and (b) measured phase shift between Δp and Δu (9). U_1 and U_2 are the MPPT voltages from Fig.9.

ripple as the experimental converter, at the temperature of $T = 27\,^{\circ}\mathrm{C}$.

1) Convergence time: The convergence time has been tested with three integral gains γ and a sequence of irradiation transients. Table II reports the sequence, the measured times T_s and the expected times T (29) calculated using the MPP locus in Fig.9. The first order HPFs have cut-off frequency $\omega_{HPF} = 2\pi(3f_{SW})$, while the second order LPF is the cascade of two first order cells with cut-off $\omega_{LPF} = 2\pi 12000\,\mathrm{rad/s}$, as in the experimental board. Fig.11 shows the simulated response to the sequence of transients. Examining table II, the correspondence between theoretical and simulated measured time can be appreciated. The errors are due to the unmodelled dynamics like the LPF and G(s). The high error in the intermediate transient (500 to $1000\,\mathrm{W/m^2}$) is due to the small voltage variation required to get into the new MPP. Fig.11 shows the duty cycle during the transients and offers a first insight on the chattering effect, as it changes with the operating point and with γ: in fact, the differential resistance r of the PV module affects $G(s)$, influencing the chattering conditions.

2) Chattering: Writing $G(s)$ from the parameters in table I, (36) can be numerically solved for the voltages corresponding to the MPP locus in Fig.9, giving the expected chattering frequency ω_C in each MPP point, depending only on the point and on the filters, and the corresponding amplitude U, depending also on γ. The results are reported in Fig.12, showing the chattering frequency f_C and the correspondent chattering

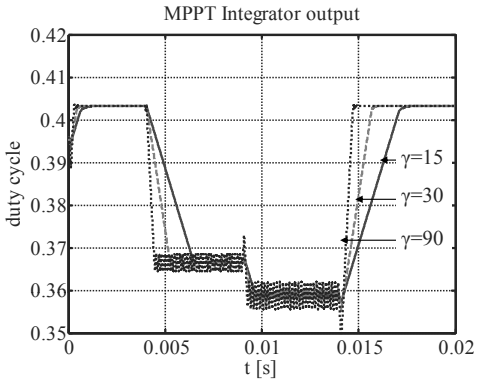

Fig. 11. Simulated duty cycle response to the step sequence in Table II for $\gamma = 15$ (continuous line) $\gamma = 30$ (dashed line) $\gamma = 90$ (dotted line).

Table II
SIMULATED CONVERGENCE TIMES T_s COMPARED WITH T FROM (29) FOR DIFFERENT VALUES OF γ AND $f_{LPF} = 12\,\mathrm{kHz}$

Transient $\mathrm{W/m^2}$	$200-500$	$500-1000$	$1000-200$
Time ms	4	9	14
$\lvert U_{MPP,f} - U_{MPP,i}\rvert$ V	0.8	0.2	1
T_s if $\gamma = 15$	2.469 ms	0.841 ms	3.011 ms
T if $\gamma = 15$	2.200 ms	0.556 ms	2.800 ms
T_s if $\gamma = 30$	1.254 ms	0.498 ms	1.583 ms
T if $\gamma = 30$	1.100 ms	0.278 ms	1.400 ms
T_s if $\gamma = 90$	0.430 ms	0.302 ms	0.519 ms
T if $\gamma = 90$	0.370 ms	0.093 ms	0.463 ms

amplitude U at the MPP as a function of the irradiation. Note that, for the particular $G(s)$, the chattering frequency has a small variation with irradiation, as well as the amplitude, that mainly depends on γ. To validate the analysis, table III shows a good agreement between the chattering predicted as a limit cycle with the simplified model in Fig.7 and the results given by the simulink model. In some conditions, the model predicts a chattering that in the time-domain simulation does not appear, making the prediction a worst case scenario that is useful for design purposes.

Table III
SIMULATED AND EXPECTED CHATTERING @ $1000\,\mathrm{W/m^2}$.

Integral gain	Expected	Simulated
$\gamma = 15$	$f_C = 6.186\,\mathrm{kHz}$	No chattering
	$U = 11.8\,\mathrm{mV}$	No chattering
$\gamma = 30$	$f_C = 6.186\,\mathrm{kHz}$	$f_C = 6.3\,\mathrm{kHz}$
	$U = 71.0\,\mathrm{mV}$	$U = 70\,\mathrm{mV}$
$\gamma = 90$	$f_C = 6.186\,\mathrm{kHz}$	$f_C = 6.3\,\mathrm{kHz}$
	$U = 23.6\,\mathrm{mV}$	$U = 20\,\mathrm{mV}$

3) Effect of LPF on convergence and chattering: The LPF has to attenuate the AC ripple after correlation, to fulfil the hypothesis on which the convergence time definition is based. Increasing the attenuation tends to increase the phase shift at lower frequencies, lowering ω_C from (36). And lower ω_C causes higher chattering amplitude from (35). The impact on chattering can be analytically evaluated plotting the same curves in Fig.12 with fixed $\gamma = 30$ and varying the cut-off frequency of the second order LPF ω_{LPF} in the set $\omega_{SET} = \{0.6, 1.8, 5.4, 12, 36, 108\}\,\mathrm{kHz}$, reported in Fig.13 in the MPPs corresponding to the experimental irradiation levels $280\,\mathrm{W/m^2}$ and $680\,\mathrm{W/m^2}$. To conclude, Fig.14 shows the

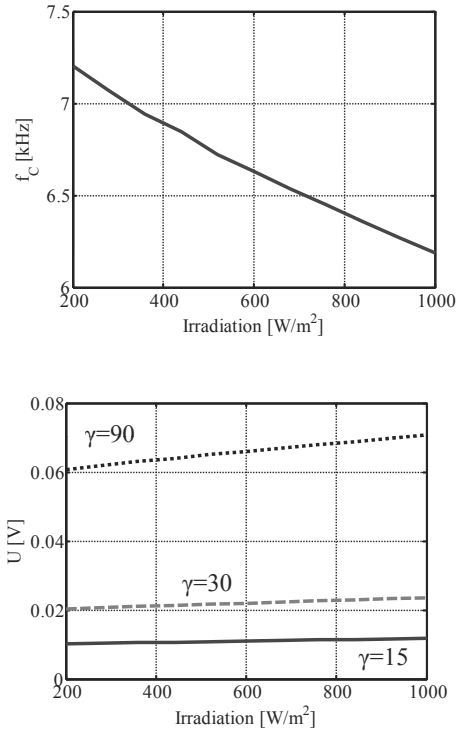

Fig. 12. Chattering conditions (35) and (36) (top and bottom) solved in the MPP locus as the irradiation varies from 200 to 1000 $\mathrm{W/m^2}$ and $T = 27°\mathrm{C}$.

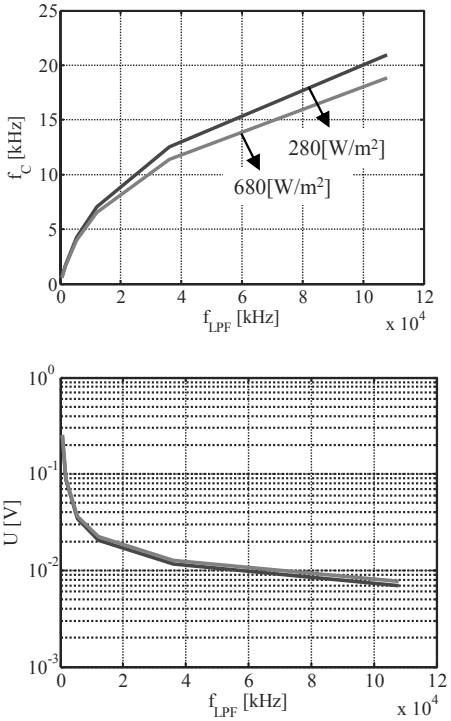

Fig. 13. Chattering conditions (35) and (36) (top and bottom) solved for $\gamma = 30$ in the MPP at 280 and 680 $\mathrm{W/m^2}$ as a function of f_{LPF}.

transient response for a $280 \rightarrow 680\,\mathrm{W/m^2}$ irradiation step. The expected convergence time can be calculated from (29) using the information from the MPP locus and is equal to $T = 0.7917\,\mathrm{ms}$. It can be seen that an high cut-off frequency moves the RCC-MPPT out of the sliding-mode, showing a first order response. Decreasing the filter frequency the response reaches the expected convergence time ($T_s = 1\,\mathrm{ms}$ measured in simulation) with $f_{LPF} = 12\,\mathrm{kHz}$ without chattering while a further reduction f_{LPF} only increases the chattering.

D. Experimental results

1) Effect of reactive parasitics: The theoretical analyses of convergence and chattering assume negligible parasitics, but the evidences in Fig.10b prove that the parasitics are far from being negligible and they play a major role in the $p-u$ transfer function. In fact, the equilibrium point corresponding to a phase equal to $-\pi/2\,\mathrm{rad}$ moves far from the theoretical MPP voltages U_1 and U_2. This result was expected also from (12), observing that ω_0 and ω_{AC} have the same order of magnitude. To partially compensate for the parasitics and enable the experimental validation of the convergence analysis, a fixed phase shift was introduced in the HPFs to guarantee the ideal MPP when $I_{SH} = I_{SH2} = 1.7\,\mathrm{A}$. The MPP was reached by $\Delta\varphi = \varphi_{HPF1} - \varphi_{HPF2} = -52°$, obtained by shifting the cut-off frequency of HPF_1 (power ripple) with respect to HPF_2 (voltage ripple). With the original cut-off $\omega_{HPF} = 2\pi(3f_{SW})$, the phase at ω_{AC} is $\varphi_{HPF_1}(\omega_{AC}) = \varphi_{HPF_2}(\omega_{AC}) = 71.56°$. To achieve the desired phase shift, the cut-off of the power filter was reduced to $\omega_{HPF_1} = 2\pi(0.315f_{SW})$, while $\omega_{HPF_2} = 2\pi(3f_{SW})$. Conversely, the LPF was the same as the one used in simulation, i.e. a second order with $f_{LPF} = 12\,\mathrm{kHz}$. This compensation is effective only when $I_{SH} = 1.7\,\mathrm{A}$. In the other experimental condition, where $I_{SH} = 0.7\,\mathrm{A}$, the system will not be able to reach the true MPP, but the convergence and the chattering can still be validated, knowing the voltage corresponding to the wrong MPP. Adding in Fig.10b the HPFs phase shift, the expected wrong equilibrium voltage will be $U_{WR} = 16.24\,\mathrm{V}$, corresponding to a power $P_{WR} = 8.42\,\mathrm{W}$, 7.5% less than the ideal maximum power. Despite the error, the results validate the analysis by confirming, at the same time, the critical influence of the parasitics in the RCC-MPPT. Having in mind the above considerations, the Fig.9 returns a voltage step during the transient of $\Delta U = 16.24 - 15.44 = 0.8\,\mathrm{V}$. Table IV reports the convergence

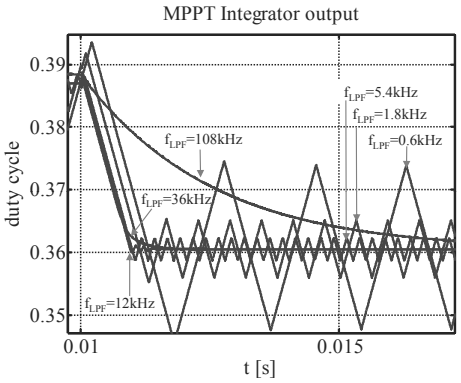

Fig. 14. Sliding mode RCC-MPPT response to a $280 \rightarrow 680\,\mathrm{W/m^2}$ irradiation step with $\gamma = 30$ for different values of f_{LPF}.

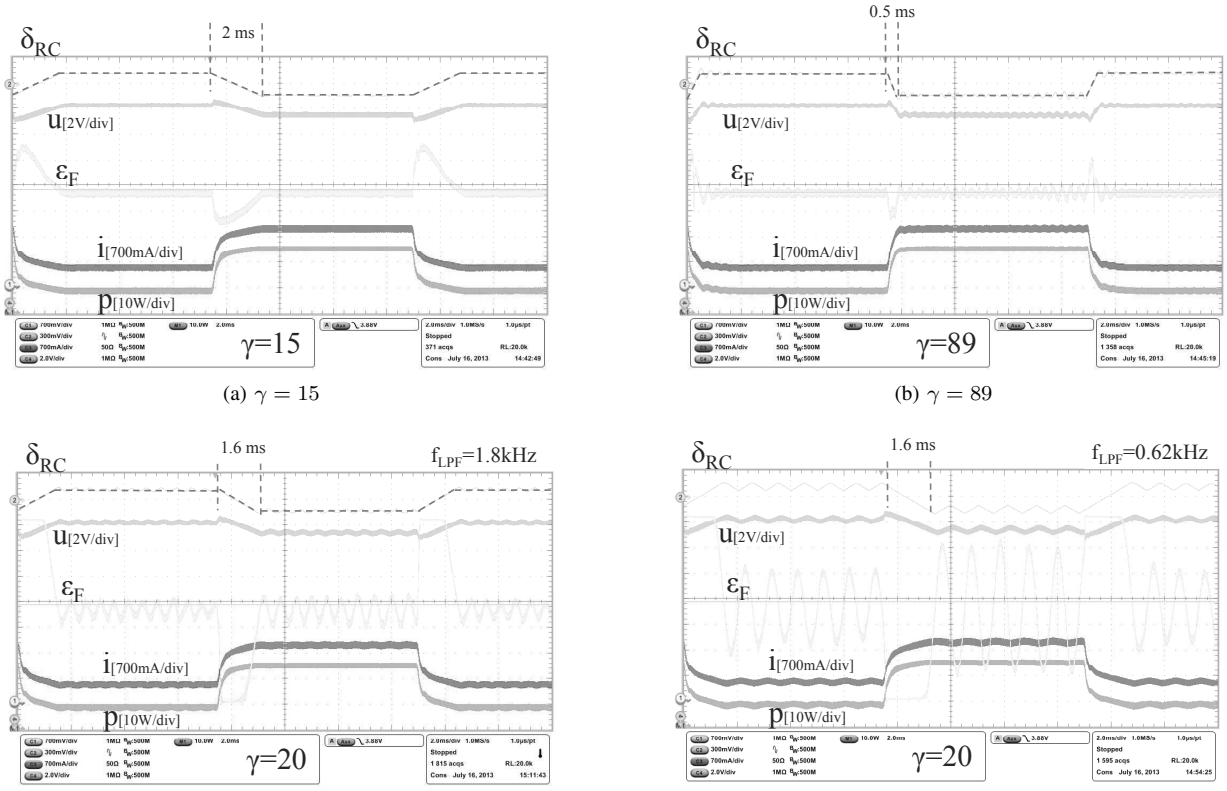

(a) $\gamma = 15$ (b) $\gamma = 89$

(c) $f_{LPF} = 1.8\,\mathrm{kHz}$ (d) $f_{LPF} = 0.62\,\mathrm{kHz}$

Fig. 15. Experimental transient response to the irradiation step $280 \rightarrow 680\,\mathrm{W/m^2}$ @ $27°$.

times expected from (29), which have to be compared with the corresponding experimental waveforms of Fig.15a and Fig.15b, showing a good agreement with the predicted data. The final results in Fig.15c and Fig.15d validate the chattering analysis providing a set of transients $280 \rightarrow 680\,\mathrm{W/m^2}$ where the integral gain is kept constant to $\gamma = 20$ and the LPF varies. The behaviour observed in the experimental setup reflects the analytical expectations: exceeding in the reduction of the cut-off frequency, the chattering phenomenon dominates, reducing the effectiveness of the MPPT. Observe that the approximated chattering prediction made in Sect.V can be applied also to the experimental setup, adding to $G(s)$ the estimated reactive parasitics L_P and C_P. Redrawing Fig.13 for $\gamma = 20$ and irradiation $680\,\mathrm{W/m^2}$, it is possible to compare the approximated chattering prediction and the experimentally measured chattering. Table V reports the comparison between the expected chattering and the measured one at $680\,\mathrm{W/m^2}$, confirming that the prediction provides a valuable even if approximated tool to estimate the chattering.

Table IV
EXPECTED CONVERGENCE TIME T FROM (29) FOR DIFFERENT VALUES OF γ AND $f_{LPF} = 12\,\mathrm{kHz}$ - EXPERIMENTAL SETUP.

Transient $\mathrm{W/m^2}$	$280 - 680$
$\lvert U_{MPP,f} - U_{MPP,i} \rvert$ V	0.8
T if $\gamma = 15$	2.2 ms
T if $\gamma = 89$	0.374 ms

Table V
PREDICTED AND MEASURED CHATTERING AT $680\,\mathrm{W/m^2}$ FOR THE LPFS IN FIG.15C AND FIG.15D.

Condition	Frequency kHz	Amplitude V
$f_{LPF} = 0.62\,\mathrm{kHz} - predicted$	0.59	0.25
$f_{LPF} = 1.8\,\mathrm{kHz} - predicted$	1.6	0.09
$f_{LPF} = 0.62\,\mathrm{kHz} - measured$	0.9	0.18
$f_{LPF} = 1.8\,\mathrm{kHz} - measured$	1.59	0.08

VII. SUMMARY

The design steps for the practical implementation of the proposed sliding-mode RCC-MPPT can be summarized as follows:

- Step 1: An approximated characterisation of the MPPT locus of the PV module is required by (30). The relevant information is the interval of MPP voltages where a controlled convergence time is desired.
- Step 2: An estimation of L_P and C_P is needed to set the maximum allowable switching frequency. A possible implementation is described in Sect.VI. The information could be limited to the order of magnitude, as a safety margin is necessary anyway.
- Step 3: The switching frequency limit is used to design the boost converter. Subsequently, the boost transfer function $G(s)$ is known.
- Step 4: The dynamic performances specification sets the convergence time limit T_{MAX}. For the hypothesis of negligible effect of $G(s)$ to be valid in the transient response, it must be $1/T_{MAX} << f_G$, where f_G is the

resonance frequency of the boost filter. The gain γ is calculated by (30).

- Step 5: The HPFs have to approximate a derivative behaviour at ω_{AC}, therefore $\omega_{HPF} > \omega_{AC}$.
- Step 6: Once defined the maximum allowed chattering, the LPF can be designed as shown in Sect.V, using the information on $G(s)$ and γ.

VIII. Conclusions

The paper proposes a detailed dynamic analysis of a sliding-mode RCC-MPPT scheme. The goal is to provide a set of design guidelines useful to develop and tune the MPPT controller to guarantee a desired dynamic behaviour in response to irradiation transients. This can be translated into an upper bound for the convergence time that is always respected by a set of relevant transients. Convergence time modelling and stability have been developed based on sliding-mode theory. Chattering effect has been modelled and included in the design, as it might reduce the effectiveness of the MPPT. Also the presence of reactive parasitics of the PV module has been included in the analysis, showing their detrimental effect on the controller. The analysis and design process have been validated with a combination of simulations and experimental results with a single PV module charging a lead-acid battery, showing a good match with the theoretical models both for convergence time and chattering.

References

[1] D. Sera, R. Teodorescu, J. Hantschel, and M. Knoll, "Optimized maximum power point tracker for fast-changing environmental conditions," *IEEE Trans. Ind. Electron.*, vol. 55, no. 7, pp. 2629–2637, 2008.

[2] J. Connors, "On the subject of solar vehicles and the benefits of the technology," in *Proc. of ICCEP '07*, May 2007, pp. 700–705.

[3] N. Fermia, D. Granozio, G. Petrone, and M. Vitelli, "Predictive adaptive MPPT perturb and observe method," *IEEE Trans. Aerosp. Electron. Syst.*, vol. 43, no. 3, pp. 934–950, July 2007.

[4] N. Femia, G. Petrone, G. Spagnuolo, and M. Vitelli, "Optimization of perturb and observe maximum power point tracking method," *IEEE Trans. Power Electron.*, vol. 20, no. 4, pp. 963–973, 2005.

[5] W. J. A. Teulings, J.-C. Marpinard, A. Capel, and D. O'Sullivan, "A new maximum power point tracking system," in *Proc. of PESC '93 Record*, Jun 1993, pp. 833–838.

[6] A. F. Boehringer, "Self-adapting dc converter for solar spacecraft power supply," *IEEE Trans. Aerosp. Electron. Syst.*, vol. AES-4, no. 1, pp. 102–111, Jan 1968.

[7] M. A. S. Masoum, H. Dehbonei, and E. Fuchs, "Theoretical and experimental analyses of photovoltaic systems with voltage and current-based maximum power-point tracking," *IEEE Trans. Energy Convers.*, vol. 17, no. 4, pp. 514–522, Dec 2002.

[8] P. Krein, "Ripple correlation control, with some applications," in *Proc. of ISCAS '99*, vol. 5, 1999, pp. 283–286.

[9] T. Esram and P. Chapman, "Comparison of photovoltaic array maximum power point tracking techniques," *IEEE Trans. Energy Convers.*, vol. 22, no. 2, pp. 439–449, 2007.

[10] M. de Brito, L. Galotto, L. Sampaio, G. de Azevedo e Melo, and C. Canesin, "Evaluation of the main MPPT techniques for photovoltaic applications," *IEEE Trans. Ind. Electron.*, vol. 60, no. 3, pp. 1156–1167, 2013.

[11] S. Jain and V. Agarwal, "Comparison of the performance of maximum power point tracking schemes applied to single-stage grid-connected photovoltaic systems," *Electric Power Applications, IET*, vol. 1, no. 5, pp. 753–762, 2007.

[12] P. Midya, P. Krein, R. Turnbull, R. Reppa, and J. Kimball, "Dynamic maximum power point tracker for photovoltaic applications," in *Proc. of PESC '96*, vol. 2, Jun 1996, pp. 1710–1716.

[13] T. Esram, J. Kimball, P. Krein, P. Chapman, and P. Midya, "Dynamic maximum power point tracking of photovoltaic arrays using ripple correlation control," *IEEE Trans. Power Electron.*, vol. 21, no. 5, pp. 1282–1291, 2006.

[14] J. Kimball and P. Krein, "Discrete-time ripple correlation control for maximum power point tracking," *IEEE Trans. Power Electron.*, vol. 23, no. 5, pp. 2353–2362, 2008.

[15] R. Leyva, C. Alonso, I. Queinnec, A. Cid-Pastor, D. Lagrange, and L. Martinez-Salamero, "MPPT of photovoltaic systems using extremum - seeking control," *IEEE Trans. Aerosp. Electron. Syst.*, vol. 42, no. 1, pp. 249–258, 2006.

[16] J. Wells, P. Chapman, and P. Krein, "Fundamental aspects of ripple correlation control of electric machinery," in *Proc. of PESC '03*, vol. 4, June 2003, pp. 1659–1662.

[17] D. Casadei, G. Grandi, and C. Rossi, "Single-phase single-stage photovoltaic generation system based on a ripple correlation control maximum power point tracking," *IEEE Trans. Energy Convers.*, vol. 21, no. 2, pp. 562–568, 2006.

[18] Y. H. Lim and D. Hamill, "Synthesis, simulation and experimental verification of a maximum power point tracker from nonlinear dynamics," in *Proc. of PESC 2001*, vol. 1, 2001, pp. 199–204.

[19] G. Spiazzi, S. Buso, and P. Mattavelli, "Analysis of MPPT algorithms for photovoltaic panels based on ripple correlation techniques in presence of parasitic components," in *Proc. of COBEP '09*, Sept 2009, pp. 88–95.

[20] J. P. Barbot and W. Perruquettil, *Sliding Mode Control in Engineering*. Marcel Dekker Inc, ISBN 0-8247-0671-4, New York, 2002.

[21] S. Buso, G. Spiazzi, and M. Meneghini, "Laboratory PV generator for MPPT dynamic response testing," in *Proc. of COBEP'13*, Oct 2013, pp. 563–568.

Alessandro Cosabeber (S'09-M'13) received the Ph.D. degree from the University of Padova, Italy, in 2012. In 2014 he joined the PEMC group, Department of Electrical and Electronic Engineering, University of Nottingham, Nottingham, UK as Lecturer in Power Electronics. In 2011, he was a visiting researcher in the PEMC group, University of Nottingham, and in 2012 he visited the GASI Group, UNESP, São Paulo, Brazil. His research interests include modelling and control of power converters, power electronics and control for distributed and renewable energy sources, HVDC converters and stability of AC and DC microgrids. Dr. Costabeber received the IEEE Joseph John Suozzi INTELEC Fellowship Award in Power Electronics in 2011.

Matteo Carraro received the M.Sc. degree in Automation Engineering and the Ph.D. degree in Mechatronics Engineering from the University of Padova, Padova, Italy, in 2010 and 2014 respectively. He is currently working for a private company and his main research interests are in advanced control algorithms and self commissioning strategies for AC motor drives. He is currently working for a private company with main research interests in advanced control algorithms and self commissioning strategies for AC motor drives.

Mauro Zigliotto (M '98) is a native of Vicenza, Italy. He is full professor of Electrical Machines and Drives at University of Padova, Italy and head of the Electric Drives Laboratory in Vicenza, Italy. Advanced control strategies and self-commisioning for ac motors are Prof. Zigliotto's main research interests. He is the secretary of the IEEE IAS-IES-PELS North Italy Joint Chapter.